Front. Earth Sci. 2022, 16(3): 541–556
https://doi.org/10.1007/s11707-021-0912-y

RESEARCH ARTICLE

# Determination of gas adsorption capacity in organic-rich marine shale: a case study of Wufeng-Lower Longmaxi Shale in the southeast Sichuan Basin

**Yingchun GUO (✉)[1,2], Pengwei WANG[3], Xiao CHEN[4], Xinxin FANG[1]**

1 Key Laboratory of Paleomagnetism and Tectonic Reconstruction, Ministry of Natural Resources, Institute of Geomechanics,
Chinese Academy of Geological Sciences, Beijing 100081, China
2 Key Laboratory of Petroleum Resources Research, Institute of Geology and Geophysics, Chinese Academy of Sciences, Beijing 100029, China
3 Research Institute of Petroleum Exploration & Production, SINOPEC, Beijing 100083, China
4 CNOOC Research Institute, Beijing 100028, China

**Abstract** Determination of gas adsorption capacity under geological conditions is essential in evaluating shale gas resource potential. A quantitative determination of gas adsorption capacity was proposed through 1) investigating controlling geological factors (including both internal ones and external ones) of gas adsorption capacity in organic-rich marine shale with geochemical analysis, XRD diffraction, field-emission scanning electron microscopy, and methane sorption isotherms; 2) defining the relationship between gas adsorption capacity and single controlling factor; 3) establishing a comprehensive determination model with the consideration of all these controlling factors. The primary controlling factors of the sorption capacity for the studied $O_3w$-Lower $S_1l$ shale are TOC, illite and quartz, temperature, pressure, $R_o$, and moisture (water saturation). Specifically, TOC, thermal maturity, illite, and pressure are positively correlated with sorption capacity, whereas, quartz and temperature contribute negatively to the sorption capacity. We present the quantitative model along with application examples from the Wufeng-Lower Longmaxi Shale in the southeast Sichuan Basin, west China, to demonstrate the approach in shale gas evaluation. The result shows that the comprehensive determination model provides a good and unbiased estimate of gas adsorption capacities with a high correlation coefficient (0.96) and bell-shaped residues centered at zero.

**Keywords** gas adsorption capacity, quantitative determination, marine shale, Wufeng-Longmaxi Shale, southeast Sichuan Basin

Received January 28, 2021; accepted May 23, 2021

E-mail: cugcupgych@163.com

## 1 Introduction

One commercially-produced unconventional shale gas system is the Longmaxi Shale, which is both a source rock and reservoir rock for the Fuling gas field in China (Zou et al., 2015), representing the first major commerce shale gas discovery outside of North America. Previous studies suggest that natural gas (mostly methane) in shale occurs in different thermodynamical phases, namely, adsorbed, absorbed, and free gas (Wang et al., 2018), while absorbed gas is one of the most important components for potential sweet spots in shale reservoir. Ambrose et al. (2012) suggested that absorbed gas contributed significantly to gas-in-place (GIP) within shales, accounting for about 20%–55% of reserves.

A large number of studies show that the adsorption capacity of shales is generally controlled by multiple factors, e.g., total organic matter content (TOC), organic matter type, thermal maturity, mineral components, micropore structure, water saturation, pressure, and temperature as well (Chalmers and Bustin, 2007; Jarvie et al., 2007; Ross and Bustin, 2007, 2009; Hartwig and Schulz, 2010; Hartwig et al., 2010; Zhang et al., 2012; Tian et al., 2016). TOC has been typically regarded as the primary controlling factor for sorption capacity in marine shale, providing abundant specific surface areas and sorption sites from organic matter (Lu et al., 1995; Chalmers and Bustin, 2008; Ross and Bustin, 2009; Wang et al., 2013; Gasparik et al., 2014; Tan et al., 2014; Wang et al., 2016; Ji et al., 2019). Mineral compositions, especially clay minerals, also play an important role in sorption capacity (Ross and Bustin, 2009; Gasparik et al., 2014), e.g., illite and interbedded illite-smectite, etc., could provide certain adsorption sites for natural gas due to the small pore sizes they formed. Nano-pore volume derived from kerogen decomposition can enhance the adsorption capacity as well (Zhang et al., 2012). Water could substantially reduce the adsorption capacity by pre-occupying pore-surface of clay minerals and eliminate methane amount in the sorption phase by restricting the access to active sites since clay minerals were typically saturated with water during deposition, which can form an irreducible film on the surface (Zhang et al., 2012). Sorption capacity is also temperature and pressure-dependent. Increasing temperature contributes negatively to the sorption capacity, since methane adsorption is a typical exothermic process, whereas pressure is positively correlated with the sorption capacity because it decreases the binding energy required for methane adsorption (Raut et al., 2007).

Among the available methods for inferring the shale sorption, direct method, e.g., $CH_4$ sorption experiment expressing the relationship between adsorbed $CH_4$ capacity and gas pressure at a fixed temperature, is widely employed to describe adsorption capacity, and the Langmuir-based and supercritical Dubinin–Radushkevich-based excess adsorption models are the most popular ones. However, there are some weaknesses in adsorption capacity evaluation methods. For example, measuring adsorption capacity using sorption experiments (e.g., methane sorption isotherms) in the library is costly and time-consuming, while limited by samples, the spatial coverage and vertical resolution are two additional constraints for identifying adsorption capacity. Also, no quantitative evaluation method was available to integrate internal factors (e.g., shale composition, pore structure) and external factors (e.g., reservoir temperature and pressure) to describe the adsorption capacity of marine shale. Therefore, the primary concern in this paper is to establish a quantitative model to determine the adsorption capacity of organic-rich marine shale with the consideration of all these related factors. A discussion of the method is followed by application examples from the Wufeng-Longmaxi Shale in southeast Sichuan to illustrate adsorption capacity.

## 2 Geological setting

The Sichuan Basin, a petroliferous basin, is located in the northwest of the Yangtze meta-platform, which is bounded by the Longmen Mountains in the west, the Qiyue Mountains in the east, Daba Mountains in the north, and Daliang Mountains in the south (Fig. 1). It can be structurally divided into three units by twofold belts (Huaying Mountain and Longquan Mountain), including West Sichuan Depression, Southeast Sichuan Slope Belt, and Central Sichuan Uplift. The study area, the Fuling

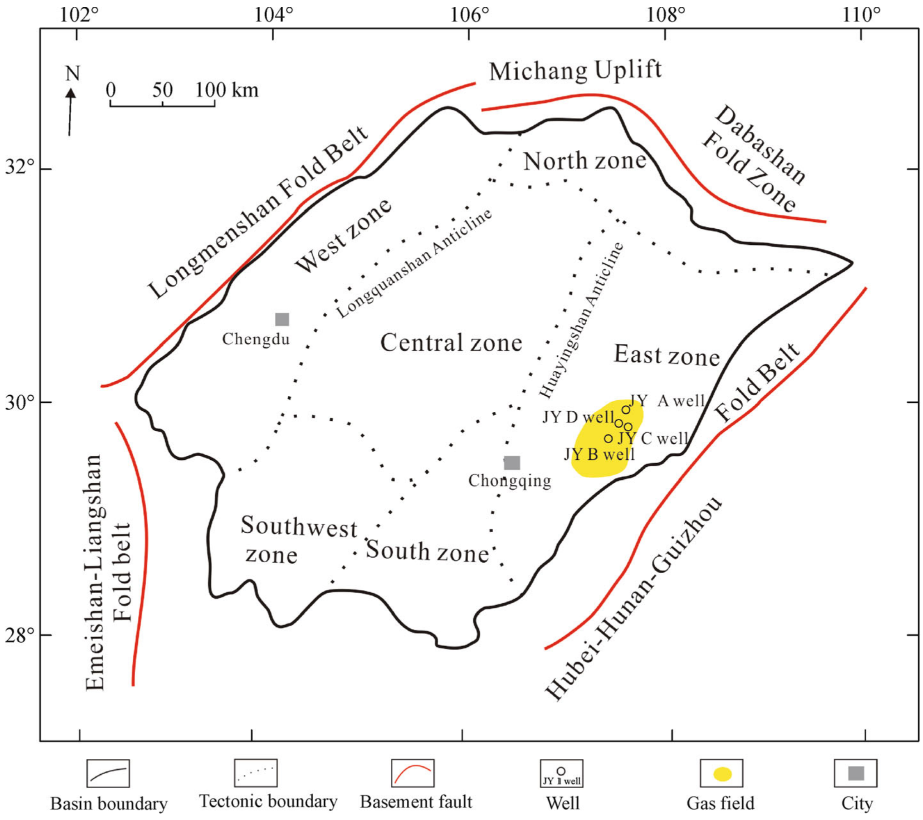

**Fig. 1** Structure units of the Sichuan Basin and location of the study area.

shale gas field in the east of Sichuan Basin, is characterized by a wide and gentle anticline confined by some high angle reverse faults, which has experienced multiple tectonic movements, e.g., Caledonian (late Sinian–Silurian), Hercynian (Devonian–Permian), Indosinian (Triassic), Yanshanian (Jurassic–Cretaceous), and Himalayan (Tertiary–Quaternary) (Li et al., 2015; Yang et al., 2016a). Slow subsidence and minor uplift occurred before the late Cretaceous, while large-scale tectonic compression and erosion caused by uplift occurred since the late Cretaceous. The Yanshanian and Himalayan movement eroded most of the Jurassic–Quaternary sequences, which is evidenced by a thin set of Jurassic sediments.

The Sichuan Basin was subsequently filled by marine carbonates, mudstones, and shales from Neoproterozoic to middle Triassic and terrestrial clastic sediments from Late Triassic to Paleogene (Fig. 2). The marine carbonates and shales from Neoproterozoic to Middle Triassic vary widely in thickness, ranging from 3500 to 6000 m. The Upper Ordovician Wufeng ($O_3w$) and Lower Silurian Longmaxi ($S_1l$) are considered as the most extensive and organic-rich shales in this petroliferous basin.

The rapid rise of global sea level during the late Ordovician and early Silurian and resulted in deep water shelf deposits in the confined paleogeography of the study area, and consequently, the low-energy and anoxic sedimentary environment deposited a successive of organic-rich $O_3w$–$S_1l$ marine shale (Yang et al., 2016a).

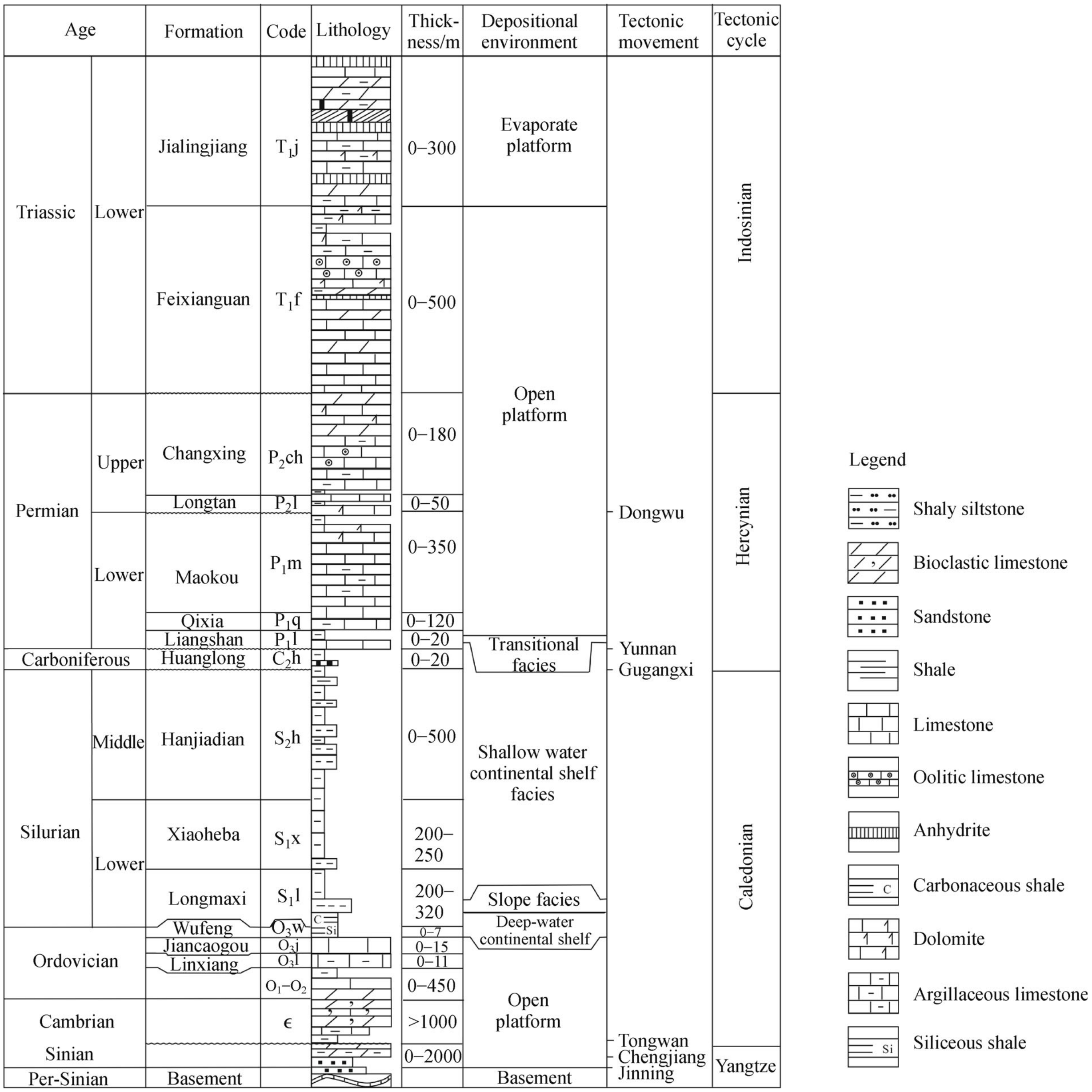

**Fig. 2** Generalized Paleozoic stratigraphic column showing related information, e.g., lithology, strata classification, and thickness (Modified from Yang et al., 2016b).

Controlled by the sedimentary environment, $O_3$w–$S_1$l marine shale varies slightly in thickness with the present-day thickness of about 60–110 m in the study area. The $O_3$w shale is mainly black fine-grained carbonaceous shale with a thickness of about 5–8 m. $S_1$l shale, overlaying conformably on the $O_3$w shale, is dominated by black shale with abundant fossils, e.g., graptolites and radiolarian, etc. (Chen et al., 2015; Yang et al., 2016a). $S_1$l shale can be subdivided into three units from bottom to top. The lower $S_1$l (60–110 m) is mainly black carbonaceous shale, carbonaceous mudstone, argillaceous siltstone, and siliceous shale. The middle section (50–100 m) is dominated by gray siltstone interbedded with dark gray argillaceous siltstone. The upper section (about 160 m) is primarily dark-gray mudstone and gray shale with fewer fossils (Yang et al., 2016b).

## 3 Samples and methods

### 3.1 Samples

In this study, a total of 92 $O_3$w–Lower $S_1$l shale samples were selected from JY A well and JY B well in the Fuling Gas Field (Fig. 1), of which 7 samples were from the $O_3$w Formation and 85 samples were from the Lower $S_1$l Formation. To comprehensively analyze the gas adsorption capacity, geochemical, mineralogical, pore geometry, $CH_4$ sorption tests were performed in the state key laboratory of shale oil and gas enrichment mechanisms and effective development in the Wuxi research institute of petroleum geology, SINOPEC.

### 3.2 Geochemical analyses

The total organic carbon contents (TOC, wt%) were measured using a LECO CS-200 carbon/sulfur analyzer. Before the measurement, 92 samples were crushed into powder with grain size < 100 mesh, and then the powder (1 g) in a porous crucible was processed using hydrochloric acid to remove carbonate and were washed using distilled water 2 h later. After the water had drained from the crucible, the crucible and powder were dried overnight at 70°C. Since no “true” vitrinite is present in the high-mature $O_3$w–Lower $S_1$l shales, random vitrinite reflectances were converted from the Bitumen vitrinite reflectance using the empirical model proposed by Schoenherr et al. (2007). Bitumen vitrinite reflectances of 9 shale samples from JY A well were measured using an MPV-III microphotometer 806 apparatus under room temperature of 23°C and relative humidity < 70%. Also, samples were processed and prepared according to the Chinese Oil and Gas Industry Standard (SY/T) 5124-2012. To make the measurement reliable, at least 10 measurements were taken on each sample whenever possible.

### 3.3 X-ray diffraction analysis

Bulk mineralogical composition and clay mineral analysis of 92 shale samples were performed on randomly oriented powders using a D8 Discover X-ray diffractometer at a working voltage of 40 kV and a current of 40 mA. Shale samples were crushed manually and powdered in ethanol for 15 min to avoid the dissolution of water-soluble minerals and make uniform crystallite sizes. Mineral quantification was conducted on diffraction patterns from random powder preparations, while sample holders were prepared with a side filling method to minimize preferential orientation. The sample was illuminated through a fixed divergence slit (1.8 mm, 1.45°), a graphite monochromator and 58 mm and 0.3 mm spacing Soller slits. The diffracted beam was measured with a scintillation detector with a counting time of 20 s for each step of 0.02° $2\theta$. Diffractograms were recorded from 2° to 76° at the rate of $2\theta$. With customized clay mineral structure models, quantitative phase analysis was performed by Rietveld refinement (Ufer et al., 2008). All reported mineral compositions related to the crystalline content of the analyzed samples.

### 3.4 Field-emission scanning electron microscopy (FE-SEM)

36 shale samples were selected for scanning electron microscopy (SEM) using an FEI Quanta 250 field emission scanning electron microscope. 20 shale samples were cut and polished in a direction normal to the bedding by an Ar-ion milling 221 instrument (Hitachi IM4000) to produce flat surfaces with a minor topographical variation. Milling was performed at accelerating voltages of 6 kV for 1.5 h and 4 kV for 0.5 h. 16 unpolished samples were observed to reveal the spatial structure of the clay minerals. Working distances during the FE-SEM observation ranged between 2.5 mm and 8 mm at a voltage of 1.5 kV. The pore diameter of nano-pores was measured using JMicroVision software. Organic pore surface area ($S_p$) and organic matter surface area ($S_o$) were measured using Image-Pro Plus 6.0 with SEM image, and thereby plane porosity ($P_p$) of organic pores was determined with the equation $P_p = S_p/S_o \times 100\%$.

### 3.5 Isothermal methane adsorption

Isothermal methane adsorption was conducted on 10 samples (4 samples from JY A well and 6 samples from JY B well) at a consistent temperature of 30°C and up to a pressure of 12 MPa using an Isothermal Adsorption Analyzer of ISO-200 and ultra-high purity (99.99%) methane as the adsorbate. To compare the impact of temperature on gas adsorption capability, a powdered shale sample with TOC of 3.47% was selected to perform adsorption experiments under 30°C, 60°C, and 90°C, respectively. 24 dry samples were crushed and sieved to less than 60 mesh particle size to reduce the influence of particle size and moisture on the sorption capacity, which were dried in a vacuum oven for 24 h at 105°C to remove moisture before the measurements. The experimental procedure was presented in detail by Zhang et al. (2012) and Hu et al. (2015). The Langmuir expression, describing the variation of adsorbed gas on a solid surface with temperature and pressure, was employed to parametrize measured adsorption data (Ross and Bustin, 2009; Zhang et al., 2012).

### 3.6 Quantitative determination model

To establish a quantitative model determining gas adsorption capacity, a general polynomial fit method was employed in this work using SPSS Statistics 17.0 software. In this study, the Langmuir volume ($Vl$), the maximum volume of gas adsorbed onto the surface area, was employed to describe the methane sorption capacity ($C_g$) of organic-rich shale. With experiments mentioned above, controlling factors were analyzed and the empirical model between $Vl$ and a single controlling factor was established. Consequently, $C_g$ was quantitatively expressed using the polynomial fit method and established empirical models (Eq. (1)).

$$C_g = a + b \times X_1 + c \times X_2 + d \times X_3 + n \times X_n, \qquad (1)$$

where, $X_1, X_2, \ldots, X_n$ are controlling factors or items related with controlling factors, $a$, $b$,…, $n$ are constants.

The principles for selecting the influencing factors of the adsorbed gas content mainly include: 1) selecting conventional and easily available parameters, 2) selecting parameters with a large amount of data, 3) selecting the one who has the most obvious impact on adsorption among the parameters related to each other. A stepwise regression method was used to establish a characterization model of the adsorbed gas content. The standard errors of different schemes were calculated, and the model with the best prediction effect (the one with the highest fitting correlation coefficient) was selected.

## 4 Results

### 4.1 TOC and thermal maturity

The measured TOC of the $O_3w$–Lower $S_1l$ shales in Fig. 3 varies significantly among different samples, which is in a range of 0.55 wt% to 5.89 wt% with an average value of 2.54 wt%. Most samples in this set are organic-rich having TOC > 2%. The bitumen reflectance values vary from 2.77% to 4.14% with an averaged value of 3.42%, correspondingly, the conversed vitrinite reflectance ($R_o$ %) is in the range 2.2%–3.1% and increases with depth, indicating over-high mature $O_3w$–Lower $S_1l$ shales (Fig. 4).

The $Vl$ values generally linearly increase with organic matter content in different $S_1l$ shale samples (Fig. 5(a)), indicating that organic matter, as a sorbent, can provide large specific surface area and sorption sites under the assumption of $CH_4$ sorption following the monolayer adsorbates theory (Hickey and Henk, 2007; Ross and Bustin, 2008). Therefore, a linear model (Eq. (2)) is employed to characterize the methane sorption capacity using TOC.

$$C_g = a \times \text{TOC} + b, \qquad (2)$$

where $a$ and $b$ are constants.

The methane sorption capacities of Lower $S_1l$ shale samples were shown to increase with maturation (Fig. 5(b)), indicating that the number of sorption sites involving the organic matter changes considerably among individual samples of different maturities. With the observation of

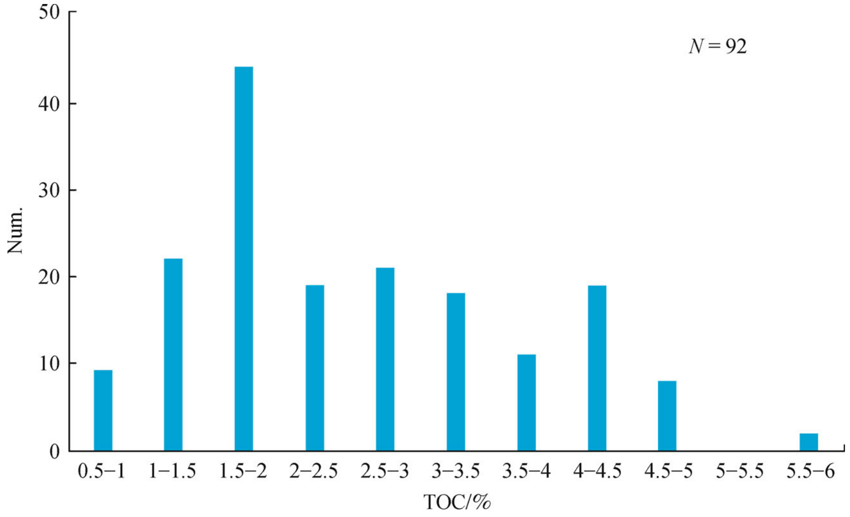

**Fig. 3** Diagrams showing Present-day TOC of the $O_3w$–Lower $S_1l$ shales.

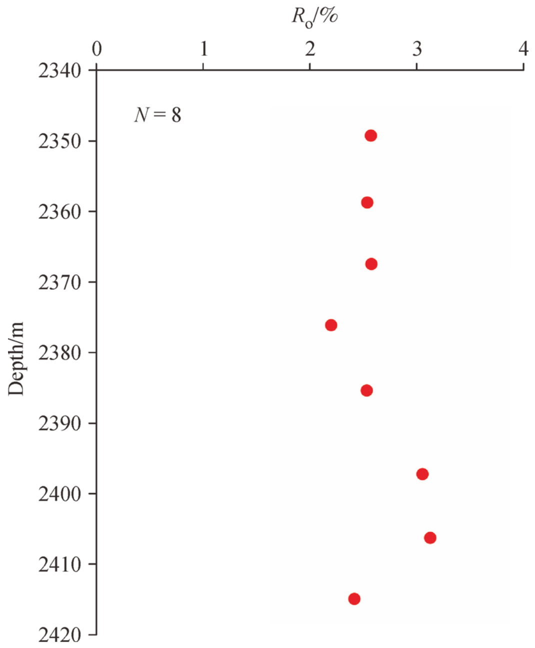

**Fig. 4** General trends of conversed vitrinite reflectance ($R_o$, %) in the $O_3$w–Lower $S_1$l shales with increasing depth.

Carboniferous samples, Gasparik et al. (2014) suggested that the sorption capacity increased considerably from immaturity to high maturity and didn't decrease after that. Zhang et al. (2012) also suggested that the sorption capacity of organic-rich shale varied greatly as a function of thermal maturation at lower pressure. Hu et al. (2015) held that the sorption capacity didn't linearly increase with thermal maturity, which grew after the oil-generation stage but almost kept unchanged before the maximum bitumen stage. Previous studies explained this increase in sorption capacity with the creation of micropores within organic matter due to the conversion of organic matter to oil and gas upon thermal maturation (Ross and Bustin, 2009; Modica and Lapierre, 2012; Milliken et al., 2013; Pommer and Milliken, 2015). Since $O_3$w–Lower $S_1$l shales are mostly over-high mature with $R_o$ values in a narrow zone (Fig. 5(b)), it is difficult to establish the relationship between the thermal maturity and *Vl* using these data. Therefore, an empirical hyperbolic model derived from (Hu, et al., 2015) (Eq. (3)) is employed to describe the impact of thermal maturity on methane sorption capacity.

$$C_g = a \times R_o/(R_o + b), \tag{3}$$

where *a* and *b* are constants.

### 4.2 Bulk mineralogy (XRD)

The comprehensive quantitative mineralogical analysis (Fig. 6(a)) shows that the $O_3$w–Lower $S_1$l shales are dominated by quartz and feldspar (23.4%–74.1%, average: 46.6%), clay mineral (16.6%–62.8%, average: 40.9%), while no significant quantities of carbonate are present in the studied samples (0–34.5%, average: 9.9%). The dominant clay mineral type is illite/smectite mixed layer and some illite, with only a small proportion of chlorite. Specifically, the illite/smectite mixed-layer content is in a range of 25%–85% with an average value of 54.45%, and illite content ranges from 12% to 68%, averaging 39.45% (Fig. 6(b)).

Figure 7(a) shows a weak negative correlation between quartz content and *Vl*, suggesting that quartz contributes minor to the methane sorption capacity. Similarly, the illite- smectite mixed-layer in the high to over-high mature organic-rich shale samples is poorly related to the methane sorption capacity. This can be explained by that the illite–smectite mixed layer can primarily enhance the sorption capacity of the low-mature shales, rather than high-mature ones (Gasparik et al., 2012; Ji et al., 2012). Different from that, illite in the Lower $S_1$l organic-rich shales is positively correlated with the *Vl* (Fig. 7(c)), suggesting that illite contributes greatly to the sorption capacity at the high-maturity stage. Previous studies explained that illite could provide additional sorption sites to high-mature organic-rich shales due to its high internal surface area (Gasparik et al., 2014; He et al., 2018).

Consequently, the quartz and illite are employed to determine the sorption capacity using a linear expression (Eqs. (4) and (5)).

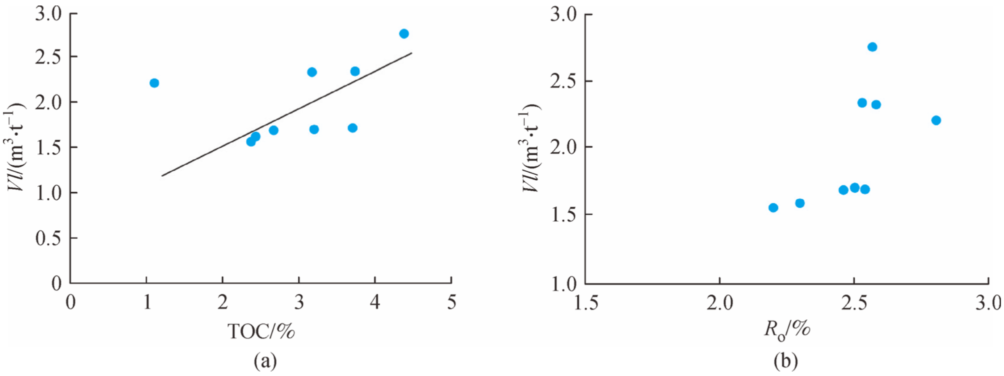

(a)

(b)

**Fig. 5** Plots of methane sorption capacities vs. TOC (a) /$R_o$ (b) for the studied samples. *Vl* is the Langmuir volume.

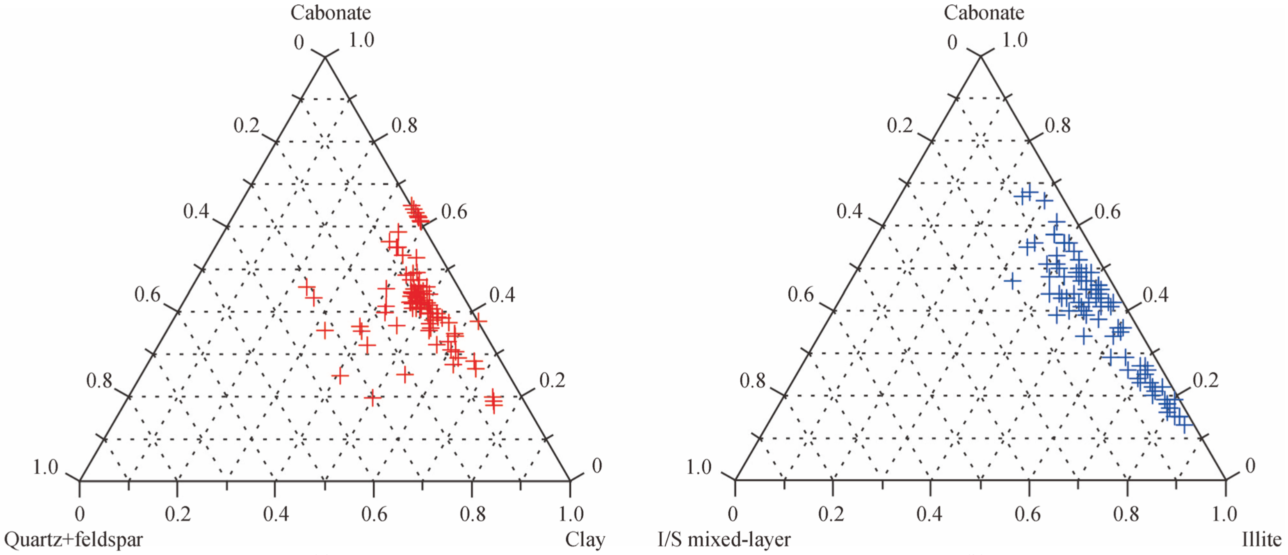

(a) (b)

**Fig. 6** Ternary diagram showing the variation in quartz and feldspar, clay mineral and carbonate contents (a) and the distribution of illite, illite/smectite mixed-layer, and chlorite (b).

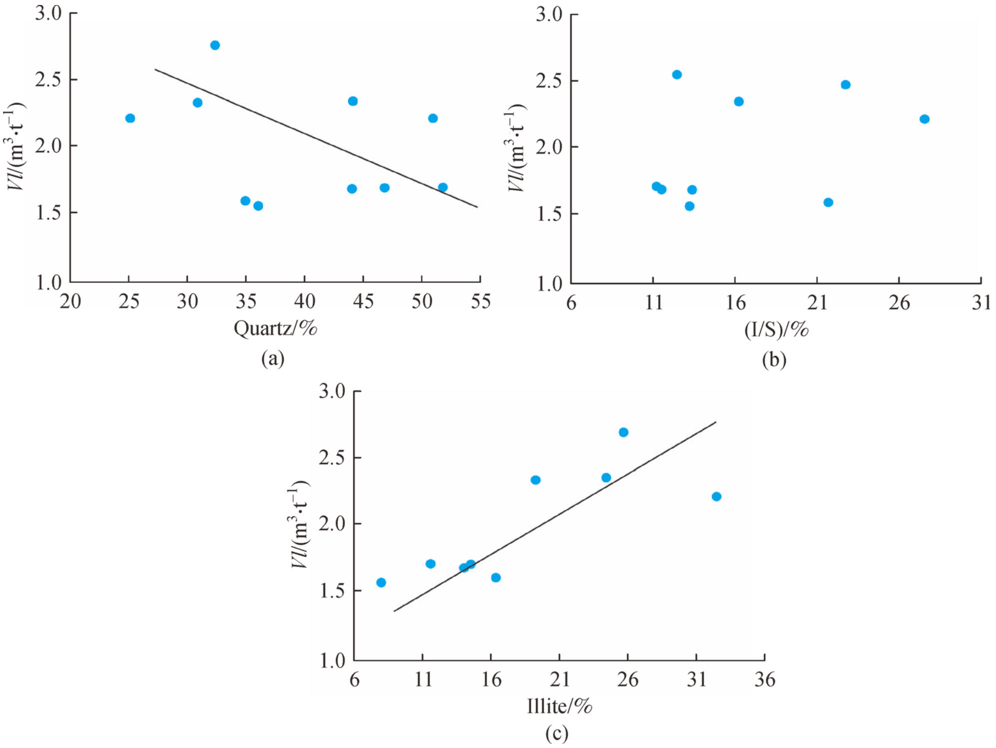

(a) (b) (c)

**Fig. 7** Plots of methane sorption capacities vs. quartz (a), illite/smectite mixed-layer (b), and illite (c) for the studied samples. *Vl* is the Langmuir volume.

$$C_g = a \times \text{quartz} + b, \tag{4}$$

$$C_g = a \times \text{illite} + b, \tag{5}$$

where $a$ and $b$ are constants.

### 4.3 Pore structure

Petrologic observations from scanning electron microscopic images suggest that the pore system in the $O_3$w–Lower $S_1$l shales is dominated by organic pores with a small proportion of matrix-hosted pores. Organic pores in the $O_3$w–Lower $S_1$l shales typically occur in the bitumen-filled space between grains. Organic pores in the Lower $S_1$l shale are commonly ellipse-like, subrounded, and rounded in shape. These pores are generally in the meso-macropore range with pore size varying significantly from 10 to 300 nm (He et al., 2018). Although in some samples, pores grew randomly in the organic matter in some samples (Fig. 8(a)), for most samples, pores are uniformly distributed in the organic matter (Figs. 8(b)–8(e)). The $O_3$w shale is dominated by abundant spongy organic pores with irregular shapes, e.g., subrounded or subangular (Fig. 8(f)). Different from the Lower $S_1$l shale, pores in the $O_3$w shale are characterized by small pore size and high density, e.g., pore size is commonly less than 50 nm.

Measured plane porosity values vary significantly among different samples. Specifically, the plot of plane porosity vs. TOC shows a positive correlation between each other, indicating that the growth of organic pores is generally governed by TOC (Fig. 9(a)). Also, the $P_p$ values change greatly within the narrow vitrinite reflectance ($R_o$, %) zone, suggesting the variation of pore sizes and numbers with thermal maturation (Fig. 9(b)) (Hackley et al., 2015).

Intragranular dissolved pores can be found in the mineral grains, which vary greatly in size (several-hundreds of nm in diameter) (Fig. 10(a)). Compared with organic pores, intragranular pores are lower in density. Intergranular pores are commonly filled by bitumen, where organic pores occur or not (Fig. 8 and Fig. 10(a)). Illite

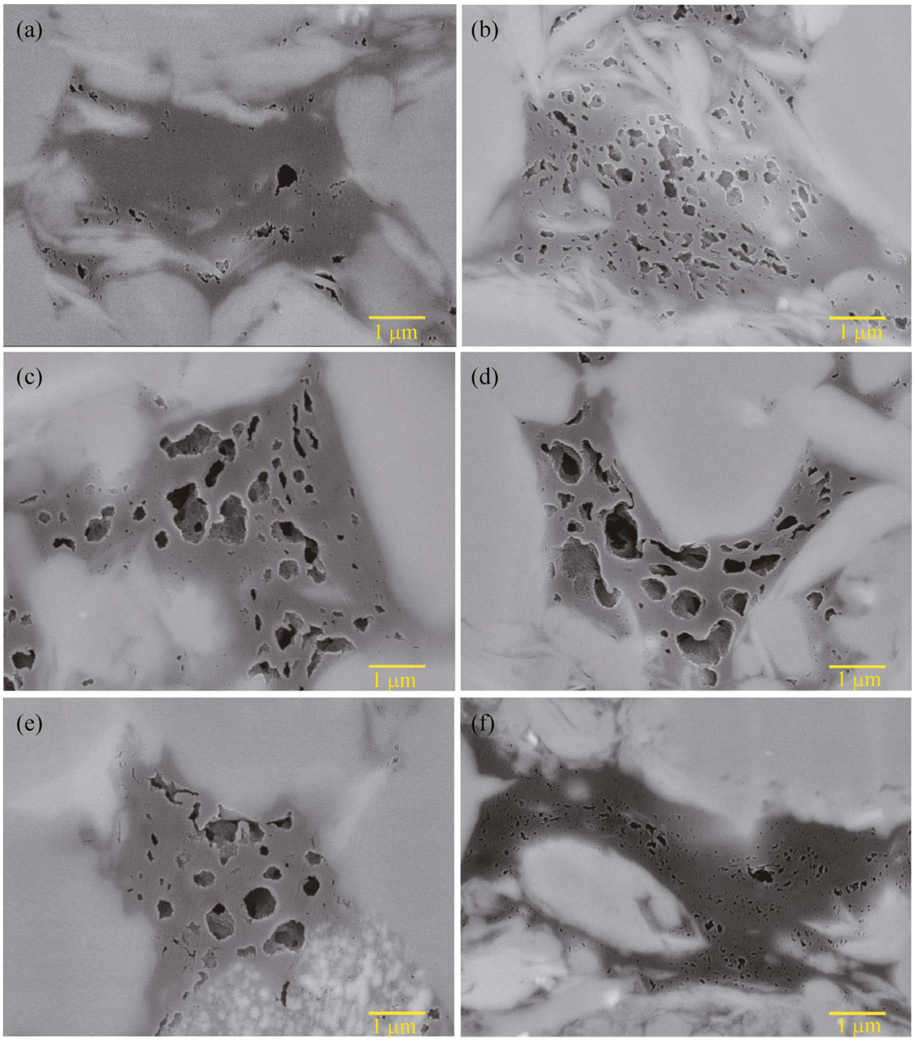

**Fig. 8** SEM images showing the variation of organic pores in the Wufeng-Longmaxi shales from the JY A well with thermal maturity and TOC. (a) Gray-black $S_1$l shale, 2339.33 m, TOC = 1.59%, $R_o$ = 2.8%, organic pores are randomly distributed and vary significantly in size; (b) gray-black $S_1$l silty mudstone, 2376.1 m, TOC = 1.59%, $R_o$ = 2.2%, pores are ellipse-like or subrounded and well-connected locally; (c) gray-black $S_1$l silty mudstone, 2385.4 m, TOC = 3.59%, $R_o$ = 2.54%; (d) gray-black $S_1$l mudstone, 2397.1 m, TOC = 3.46%, $R_o$ = 3.06%, ellipse-like pores with homogenous pore size; (e) gray-black $S_1$l mudstone, 2406.2 m, TOC = 4.77%, $R_o$ = 3.13%, rounded and subrounded organic pores; (f) gray-black $O_3$w mudstone, TOC = 4.45%, $R_o$ = 2.42%, subrounded or subangular organic pores with small pore size in the twisted kerogen.

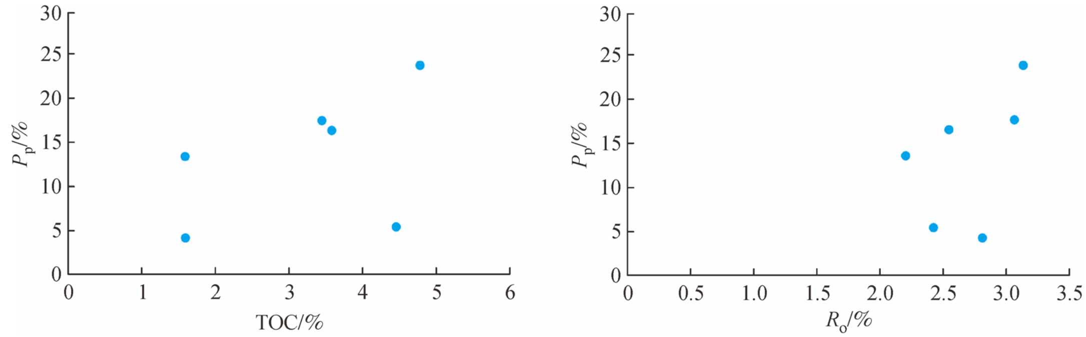

(a) (b)

**Fig. 9** Plots of Pp for organic pores vs. TOC (a) and $R_o$ (b) for the studied samples. $P_p$ represents the measured plane porosity.

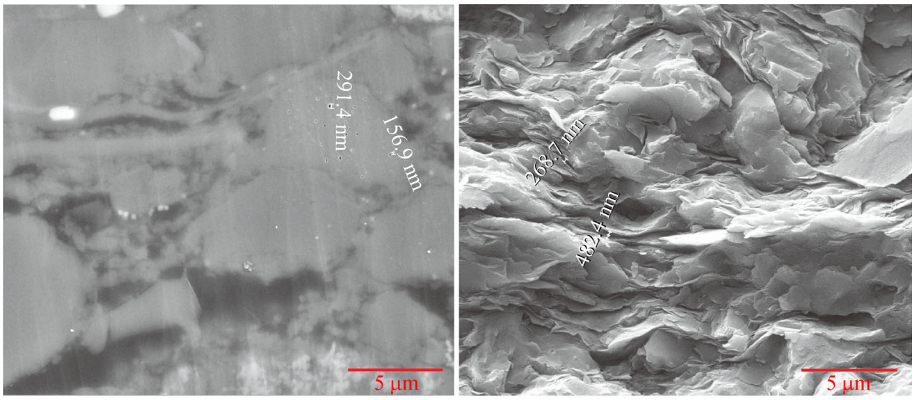

(a) (b)

**Fig. 10** SEM images showing matrix-hosted pores in the Lower $S_1$l shale. (a) Intragranular dissolved pores in the calcite grains from gray-black $S_1$l shale, bubble-like with various sizes, JY B well, 2593.7 m. (b) Illite-dominated clay mineral, abundant slit- or plate-like pores with maximum diameter up to hundreds of nanometer, JY B well, 2584.49 m.

observed from the SEM images is commonly directional arranged with slip-sheet structure (Fig. 10(b)), where a large number of nano-scale pores occur between or within Illite. These Illite-hosted pores are commonly slit- or plate-like with a rough surface and inhomogeneous pore size that is up to several hundreds of nanometer in diameter (Fig. 10(b)).

### 4.4 Methane adsorption isotherms

The methane sorption isotherms measured at 30°C on 10 studied shale samples are used to characterize the absorbed gas capacities of the $S_1$l shale as a function of TOC, thermal maturity ($R_o$, %), pressure. As Fig. 11 exhibits, methane sorption capacities of the Lower $S_1$l shale samples are typically governed by pressure. The adsorption capacities of the Lower $S_1$l shales from the JY1 well range from 1.63 to 2.2 $m^3/t$ at a relative pressure of 10.83 MPa (Fig. 11(a)), while the values of JY B samples vary from 1.54 to 1.72 $m^3/t$ (Fig. 11(b)).

Methane sorption isotherms of Lower $S_1$l shale from JY A well show the variation of methane sorption capacity with temperature (Fig. 12). In general, curves of different temperatures follow a similar trend but differ remarkably in maximum sorption value, e.g., 0.96 $m^3/t$ at 90°C, 2.01 $m^3/t$ at 60°C, and 3.03 $m^3/t$ at 30°C, indicating that methane sorption capacity decreases with increasing temperature.

The methane adsorption is commonly considered as an exothermic process that involves the physical (Van-der-Waals forces) bonding of gas and solid molecules (Gasparik et al., 2014). Methane sorption isotherms of Lower $S_1$l shale sample at different temperatures suggest that methane adsorption capacity of Lower $S_1$l shale typically decreases with increasing temperature from 30°C to 90°C, e.g., $Vl$ is 2.44 $m^3/t$ at 30°C and 0.68 $m^3/t$ at 90°C. However, limited Lower $S_1$l shale samples can’t precisely show the variation of the methane sorption capacity with increasing temperature (Fig. 13). Based on the supercritical Dubinin–Radushkevich (SDR) equation (Eq. (6)) (Schoenherr et al., 2007), the relationship between methane sorption capacity and temperature can be simplified as Eq. (7).

$$C_g = Vl \times \exp\left\{-D \times \left[\ln\left(\frac{\rho_{ads}}{\rho_g}\right) \times R \times T\right]^2\right\}, \quad (6)$$

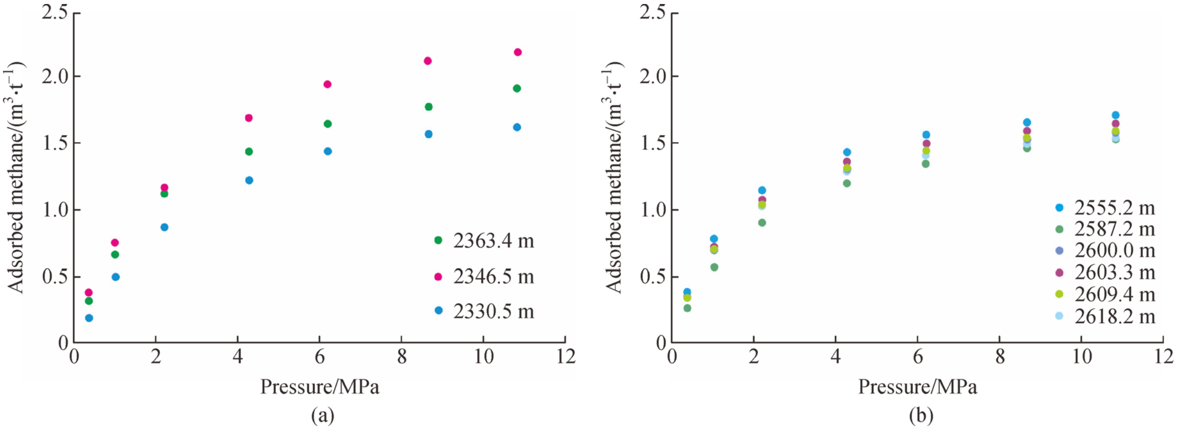

(a) (b)

**Fig. 11** Methane sorption isotherms at 30°C measured on JY A (a) and JY B (b) samples.

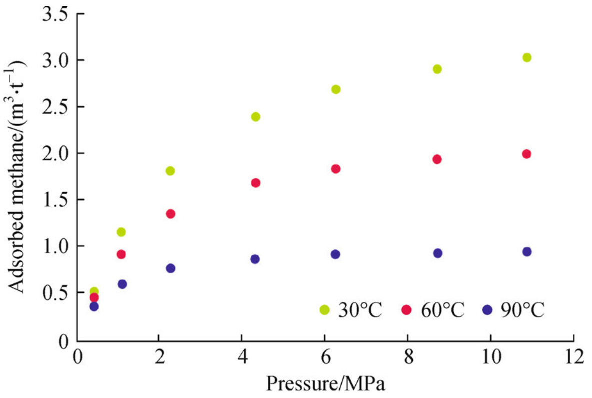

**Fig. 12** Methane sorption isotherms at different temperatures (30°C, 60°C, 90°C) measured on JY A sample.

where $D$ is a parameter involving pore structure ($\mathrm{mol}^2\cdot\mathrm{kJ}^{-2}$), $R$ is the ideal gas constant ($8.314 \times 10^{-3}$ kJ $\cdot\mathrm{mol}^{-1}\cdot\mathrm{K}^{-1}$) and $T$ is the temperature (K), $\rho_{\mathrm{ads}}$ and $\rho_{\mathrm{g}}$ are the density of methane under the adsorbed phase and methane density under certain pressure and temperature ($\mathrm{mg/cm}^3$), respectively. For a sample under fixed pressure, $D$, $\rho_{\mathrm{ads}}$, and $\rho_{\mathrm{g}}$ can be constant, then the Eq. (6) can be simplified as

$$C_{\mathrm{g}} = a \times \exp(-b \times T^2), \tag{7}$$

where $a$ and $b$ are constants.

Methane sorption capacity is also pressure-dependence. Generally, pressure positively contributes to the methane sorption capacity (Fig. 9), because high pressure can decrease the binding energy required for gas sorption. However, methane sorption capacity doesn't change anymore with increasing pressure after reaching a maximum value (Gasparik et al., 2014). Thus, the Langmuir isotherm was used to define the relationship between pressure and methane sorption capacity (Eq. (8)):

$$C_{\mathrm{g}} = a \times \frac{P}{P + P_l}. \tag{8}$$

## 5 Discussion

### 5.1 Quantitative expression of gas adsorption capacity

Based on the consideration of both internal (TOC, thermal maturity, minerals, and pore structure) and external (temperature and pressure) controls of methane sorption capacity and the empirical relationships mentioned above (Eqs. (2)–(8), Table 1), the quantitative expression of gas adsorption capacity for $\mathrm{O_3w}$–Lower $\mathrm{S_1l}$ shale was established using the Eq. (1). Thus, the data-driven model can be expressed as follows:

$$\begin{aligned} C_{\mathrm{g}} &= 0.043 \times \mathrm{TOC} + 209.92 \times \frac{R_{\mathrm{o}}}{R_{\mathrm{o}} + 0.013} \\ &\quad + 0.008 \times I \times 0.2 - 0.001 \times Q + \mathrm{e}^{-T^2} + 1.869 \\ &\quad \times \frac{P}{P + 1.898} - 209.045, \end{aligned} \tag{9}$$

where $I$ and $Q$ are illite and quartz contents, respectively (%), $T$ is the temperature (°C), $P$ is the formation pressure (MPa), $R_{\mathrm{o}}$ is the vitrinite reflectance (%). The "0.2" behind

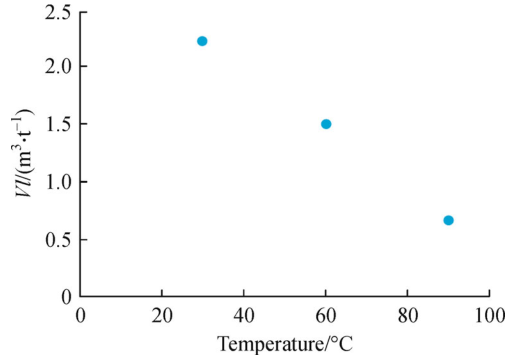

**Fig. 13** Plots of methane sorption capacities vs. temperature for the studied samples. *Vl* is the Langmuir volume.

**Table 1** The controlling factors and estimated $C_g$ with the quantitative expression (Eq. (9))

| Member | Depth/m | TOC/% | $R_o$/% | Quartz content | Illite content | $T$/°C | $P$/MPa | Estimated $C_g$/ (m$^3$·t$^{-1}$) | Field-tested $C_g$/ (m$^3$·t$^{-1}$) |
|---|---|---|---|---|---|---|---|---|---|
| S$_1$l | 2330.46 | 1.11 | 2.2 | 25.2 | 32.6 | 76.92 | 31.97 | 1.48 | 0.63 |
| S$_1$l | 2332.63 | 1 | 2.21 | 30.5 | 36.8 | 76.98 | 32.00 | 1.48 | |
| S$_1$l | 2333.98 | 0.75 | 2.22 | 29.8 | 34.2 | 77.02 | 32.02 | 1.47 | |
| S$_1$l | 2335.08 | 0.6 | 2.23 | 29.7 | 26.8 | 77.05 | 32.27 | 1.46 | |
| S$_1$l | 2335.3 | 0.78 | 2.24 | 28.2 | 29.5 | 77.05 | 32.27 | 1.48 | |
| S$_1$l | 2337.27 | 1.21 | 2.25 | 29.9 | 25.2 | 77.11 | 32.30 | 1.50 | |
| S$_1$l | 2338.2 | 1.41 | 2.26 | 18.8 | 21.0 | 77.13 | 32.31 | 1.52 | |
| S$_1$l | 2339.33 | 1.47 | 2.27 | 30.7 | 29.4 | 77.16 | 32.55 | 1.53 | |
| S$_1$l | 2340.82 | 1.59 | 2.28 | 34.2 | 20.0 | 77.20 | 32.57 | 1.52 | 0.84 |
| S$_1$l | 2341.45 | 2.19 | 2.29 | 36.8 | 9.9 | 77.22 | 32.58 | 1.53 | |
| S$_1$l | 2342.59 | 1.99 | 2.3 | 26 | 30.7 | 77.25 | 32.60 | 1.57 | 0.88 |
| S$_1$l | 2343.56 | 1.54 | 2.31 | 27.4 | 24.2 | 77.28 | 32.61 | 1.54 | |
| S$_1$l | 2344.58 | 1.87 | 2.32 | 26.3 | 23.4 | 77.30 | 32.86 | 1.56 | |
| S$_1$l | 2345.49 | 2.45 | 2.33 | 29.8 | 21.8 | 77.33 | 32.87 | 1.59 | |
| S$_1$l | 2346.5 | 2.68 | 2.34 | 32.3 | 13.8 | 77.36 | 32.88 | 1.59 | 1.08 |
| S$_1$l | 2347.46 | 2.27 | 2.35 | 31.4 | 29.5 | 77.38 | 32.90 | 1.60 | |
| S$_1$l | 2348.69 | 2.19 | 2.36 | 26.6 | 23.8 | 77.41 | 32.91 | 1.60 | 0.81 |
| S$_1$l | 2349.62 | 2.32 | 2.37 | 26.1 | 29.5 | 77.44 | 33.16 | 1.62 | |
| S$_1$l | 2351 | 1.85 | 2.38 | 18.4 | 23.2 | 77.48 | 33.18 | 1.60 | |
| S$_1$l | 2352.9 | 2.53 | 2.39 | 27.3 | 25.6 | 77.53 | 33.20 | 1.63 | |
| S$_1$l | 2354.2 | 1.29 | 2.4 | 23.5 | 15.3 | 77.56 | 33.22 | 1.57 | |
| S$_1$l | 2355.1 | 1.62 | 2.41 | 33.9 | 22.0 | 77.59 | 33.47 | 1.59 | 0.76 |
| S$_1$l | 2356.1 | 1.46 | 2.42 | 34.7 | 17.9 | 77.61 | 33.48 | 1.58 | |
| S$_1$l | 2357.1 | 1.7 | 2.43 | 33.4 | 19.4 | 77.64 | 33.49 | 1.60 | 0.86 |
| S$_1$l | 2358.1 | 1.55 | 2.44 | 33 | 22.1 | 77.67 | 33.51 | 1.60 | 0.8 |
| S$_1$l | 2359 | 1.56 | 2.45 | 34.2 | 11.2 | 77.69 | 33.52 | 1.59 | |
| S$_1$l | 2360 | 1.52 | 2.46 | 34.5 | 16.1 | 77.72 | 33.77 | 1.60 | 0.74 |
| S$_1$l | 2361 | 1.69 | 2.47 | 34 | 20.0 | 77.75 | 33.78 | 1.62 | |
| S$_1$l | 2362 | 1.51 | 2.48 | 35 | 17.2 | 77.77 | 33.80 | 1.61 | |
| S$_1$l | 2363.4 | 1.47 | 2.49 | 30.9 | 19.3 | 77.81 | 33.82 | 1.62 | |
| S$_1$l | 2364.5 | 2.12 | 2.5 | 34.4 | 20.5 | 77.84 | 33.83 | 1.65 | 0.92 |
| S$_1$l | 2365.5 | 1.57 | 2.51 | 36.3 | 21.2 | 77.87 | 34.08 | 1.63 | |

(*Continued*)

| Member | Depth/m | TOC/% | $R_o$/% | Quartz content | Illite content | $T$/°C | $P$/MPa | Estimated $C_g$/($m^3 \cdot t^{-1}$) | Field-tested $C_g$/($m^3 \cdot t^{-1}$) |
|---|---|---|---|---|---|---|---|---|---|
| $S_1$l | 2366.7 | 2.12 | 2.52 | 36.9 | 16.5 | 77.90 | 34.09 | 1.65 | 1.14 |
| $S_1$l | 2367.88 | 1.72 | 2.53 | 37.7 | 9.5 | 77.93 | 34.11 | 1.62 | |
| $S_1$l | 2368.94 | 1.8 | 2.54 | 34 | 23.4 | 77.96 | 34.13 | 1.66 | |
| $S_1$l | 2369.63 | 1.61 | 2.55 | 32.4 | 19.7 | 77.98 | 34.14 | 1.65 | 2.38 |
| $S_1$l | 2370.58 | 1.85 | 2.56 | 28.9 | 22.7 | 78.01 | 34.38 | 1.67 | |
| $S_1$l | 2371.62 | 1.44 | 2.57 | 27.7 | 30.6 | 78.03 | 34.40 | 1.67 | |
| $S_1$l | 2372.2 | 1.71 | 2.58 | 32.7 | 28.9 | 78.05 | 34.41 | 1.68 | |
| $S_1$l | 2372.58 | 1.61 | 2.59 | 31.7 | 19.5 | 78.06 | 34.64 | 1.67 | 2.69 |
| $S_1$l | 2373.52 | 1.32 | 2.6 | 31.1 | 17.8 | 78.09 | 34.66 | 1.66 | 2.83 |
| $S_1$l | 2374.28 | 1.5 | 2.61 | 32.6 | 18.4 | 78.11 | 34.90 | 1.67 | |
| $S_1$l | 2375.28 | 1.52 | 2.62 | 33.9 | 20.2 | 78.13 | 34.92 | 1.67 | |
| $S_1$l | 2376.05 | 1.83 | 2.63 | 31.1 | 19.7 | 78.15 | 34.93 | 1.69 | |
| $S_1$l | 2376.89 | 1.37 | 2.64 | 25.7 | 15.0 | 78.18 | 35.17 | 1.68 | |
| $S_1$l | 2377.69 | 2.01 | 2.65 | 34.4 | 23.5 | 78.20 | 35.65 | 1.71 | |
| $S_1$l | 2378.41 | 2.46 | 2.66 | 32.3 | 18.8 | 78.22 | 35.66 | 1.73 | 0.94 |
| $S_1$l | 2379.19 | 2.67 | 2.67 | 35.2 | 15.1 | 78.24 | 35.67 | 1.74 | |
| $S_1$l | 2380.13 | 3.22 | 2.68 | 38.2 | 17.1 | 78.26 | 35.92 | 1.76 | |
| $S_1$l | 2380.97 | 2.99 | 2.69 | 35 | 22.1 | 78.29 | 35.93 | 1.77 | |
| $S_1$l | 2381.91 | 3.01 | 2.7 | 36.8 | 12.6 | 78.31 | 35.95 | 1.76 | 2 |
| $S_1$l | 2382.67 | 3.22 | 2.71 | 40.4 | 26.3 | 78.33 | 36.19 | 1.79 | |
| $S_1$l | 2383.62 | 3.35 | 2.72 | 37.9 | 15.0 | 78.36 | 36.21 | 1.78 | 2.5 |
| $S_1$l | 2384.41 | 3.54 | 2.73 | 43.2 | 6.0 | 78.38 | 36.22 | 1.77 | |
| $S_1$l | 2385.42 | 3.59 | 2.74 | 42.2 | 16.6 | 78.41 | 36.23 | 1.80 | |
| $S_1$l | 2386.36 | 3.62 | 2.75 | 41.3 | 18.6 | 78.43 | 36.25 | 1.81 | |
| $S_1$l | 2387.65 | 3.99 | 2.76 | 47.6 | 12.7 | 78.47 | 36.27 | 1.81 | 4.04 |
| $S_1$l | 2388.52 | 3.45 | 2.77 | 46.7 | 17.2 | 78.49 | 36.28 | 1.80 | |
| $S_1$l | 2389.31 | 3.3 | 2.78 | 51.4 | 11.3 | 78.51 | 36.29 | 1.78 | |
| $S_1$l | 2390.02 | 3.42 | 2.79 | 44.3 | 19.4 | 78.53 | 36.30 | 1.81 | |
| $S_1$l | 2390.87 | 3.77 | 2.8 | 31.9 | 21.2 | 78.55 | 36.32 | 1.85 | |
| $S_1$l | 2391.95 | 3.09 | 2.81 | 36 | 9.8 | 78.58 | 36.33 | 1.80 | 2.57 |
| $S_1$l | 2392.74 | 2.24 | 2.82 | 31 | 14.3 | 78.60 | 36.35 | 1.78 | 0.89 |
| $S_1$l | 2393.6 | 2.54 | 2.83 | 38 | 15.1 | 78.63 | 36.36 | 1.79 | |
| $S_1$l | 2394.3 | 2.56 | 2.84 | 40.3 | 6.1 | 78.65 | 36.37 | 1.77 | |
| $S_1$l | 2395.3 | 2.76 | 2.85 | 41.4 | 10.6 | 78.67 | 36.38 | 1.79 | |
| $S_1$l | 2396 | 2.3 | 2.86 | 37.5 | 19.4 | 78.69 | 36.40 | 1.79 | |
| $S_1$l | 2397.1 | 3.46 | 2.87 | 42.7 | 6.3 | 78.72 | 36.41 | 1.82 | 1.08 |
| $S_1$l | 2398 | 3.95 | 2.88 | 43.6 | 8.6 | 78.75 | 36.43 | 1.85 | |
| $S_1$l | 2399 | 4.16 | 2.89 | 49.6 | 5.3 | 78.77 | 36.44 | 1.85 | |
| $S_1$l | 2400.1 | 4.12 | 2.9 | 47.1 | 5.9 | 78.80 | 36.46 | 1.85 | 1.47 |
| $S_1$l | 2400.9 | 4.11 | 2.91 | 48.9 | 7.0 | 78.82 | 36.47 | 1.86 | |
| $S_1$l | 2401.4 | 4.43 | 2.92 | 53 | 4.0 | 78.84 | 36.48 | 1.87 | |
| $S_1$l | 2402.6 | 2.94 | 2.93 | 42.3 | 4.5 | 78.87 | 36.50 | 1.82 | 4.14 |
| $S_1$l | 2403.6 | 2.99 | 2.94 | 34.6 | 5.5 | 78.90 | 36.51 | 1.83 | |
| $S_1$l | 2404.5 | 4.56 | 2.95 | 48.9 | 6.4 | 78.92 | 36.52 | 1.89 | |

(*Continued*)

| Member | Depth/m | TOC/% | $R_o$/% | Quartz content | Illite content | $T$/°C | $P$/MPa | Estimated $C_g$/ ($m^3 \cdot t^{-1}$) | Field-tested $C_g$/ ($m^3 \cdot t^{-1}$) |
|---|---|---|---|---|---|---|---|---|---|
| $S_1l$ | 2405.3 | 4.48 | 2.96 | 49.6 | 7.9 | 78.94 | 36.54 | 1.89 | 4.15 |
| $S_1l$ | 2406.2 | 4.77 | 2.97 | 51.5 | 4.2 | 78.97 | 36.55 | 1.90 | 4.96 |
| $S_1l$ | 2407.4 | 3.64 | 2.98 | 44.7 | 4.9 | 79.00 | 36.57 | 1.86 | |
| $S_1l$ | 2408 | 4.23 | 2.99 | 57.2 | 3.6 | 79.02 | 36.58 | 1.87 | |
| $O_3w$ | 2411.1 | 4.01 | 3 | 65.8 | 2.0 | 79.10 | 36.62 | 1.86 | |
| $O_3w$ | 2411.9 | 4.97 | 3.01 | 69.1 | 2.7 | 79.12 | 36.64 | 1.90 | |
| $O_3w$ | 2412.3 | 4.77 | 3.02 | 56.5 | 6.6 | 79.13 | 36.64 | 1.91 | 4.31 |
| $O_3w$ | 2413.1 | 4.03 | 3.03 | 70.6 | 4.2 | 79.15 | 36.65 | 1.86 | |
| $O_3w$ | 2414.2 | 4.46 | 3.04 | 55.7 | 8.3 | 79.18 | 36.67 | 1.91 | |
| $O_3w$ | 2414.9 | 4.45 | 3.05 | 32.8 | 24.6 | 79.20 | 36.68 | 1.96 | 3.55 |

illite represents the influence of moisture on the sorption capacity.

The estimated $C_g$ values from the determination model with the fitted empirical relationships are in good agreement with the measured $C_g$ through isothermal methane adsorption with a correlation coefficient of 0.96, indicating that the determination model can provide closer matches with the measured ones (Fig. 14(a)). The residuals, defined as the difference between the predicted and observed $C_g$, show bell-shaped distribution with means close to zeros, indicating unbiased estimations. So good agreement reflects that the formula we have established is reasonable.

We present examples of determining methane sorption capacity for the $O_3w$–Lower $S_1l$ shale in the JY A well with Eq. (9). Predicted $C_g$s vary from 1.46 to 1.96 $m^3/t$, with average value of 1.70 $m^3/t$. Because of a narrow depth range (2330–2415 m), the temperature and formation pressure doesn't change obviously. Though they both have controls on the sorption capacity, they cannot cause a clear change trend of gas sorption capacity. The control of illite and quartz on the estimated $C_g$ trend is seemingly contrary to that in Eq. (9). The reason is that the illite and quartz have a negligible effect compared to TOC, $P$, and $T$. Thus, the changing trend between adsorbed gas and illite and quartz is not obvious. However, the small-scale changes of illite and quartz in Fig. 15 (2390–2392 m) can reflect their real effect. The field-tested $C_g$ is listed in Fig. 15, and it has a similar trend with the estimated $C_g$, indicating the result is acceptable. Because field-tested $C_g$ is the sum of free gas and adsorbed gas and the amount of adsorbed gas cannot be determined. So, our next work is to establish a free gas prediction formula to compare the specific values between estimated and field-tested gas contents.

### 5.2 Impact of other geological factors on methane sorption capacity

Methane adsorption in shale is the result of gas-liquid-solid interaction when considering water saturation in actual condition. The moisture (water saturation) which significantly influences methane adsorption capacity will likely misestimate the shale gas resources (Chalmers and Bustin, 2008; Ross and Bustin, 2009). However, the distribution of water is significantly controlled by pore size, the interaction among methane, water film, and minerals, e.g., clay

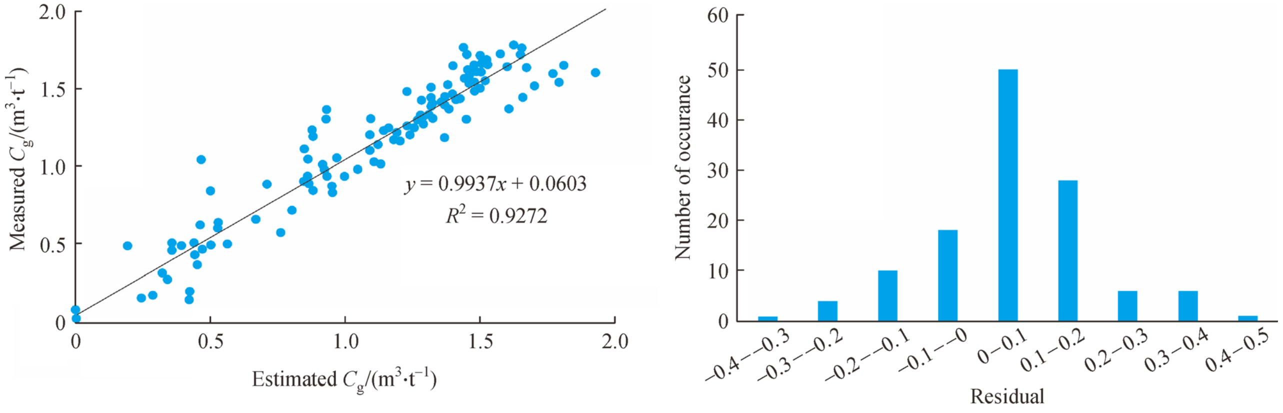

(a) (b)

**Fig. 14** Comparison of (a) estimated gas adsorption capacity ($C_g$) and (b) measurementsand the residual distribution.

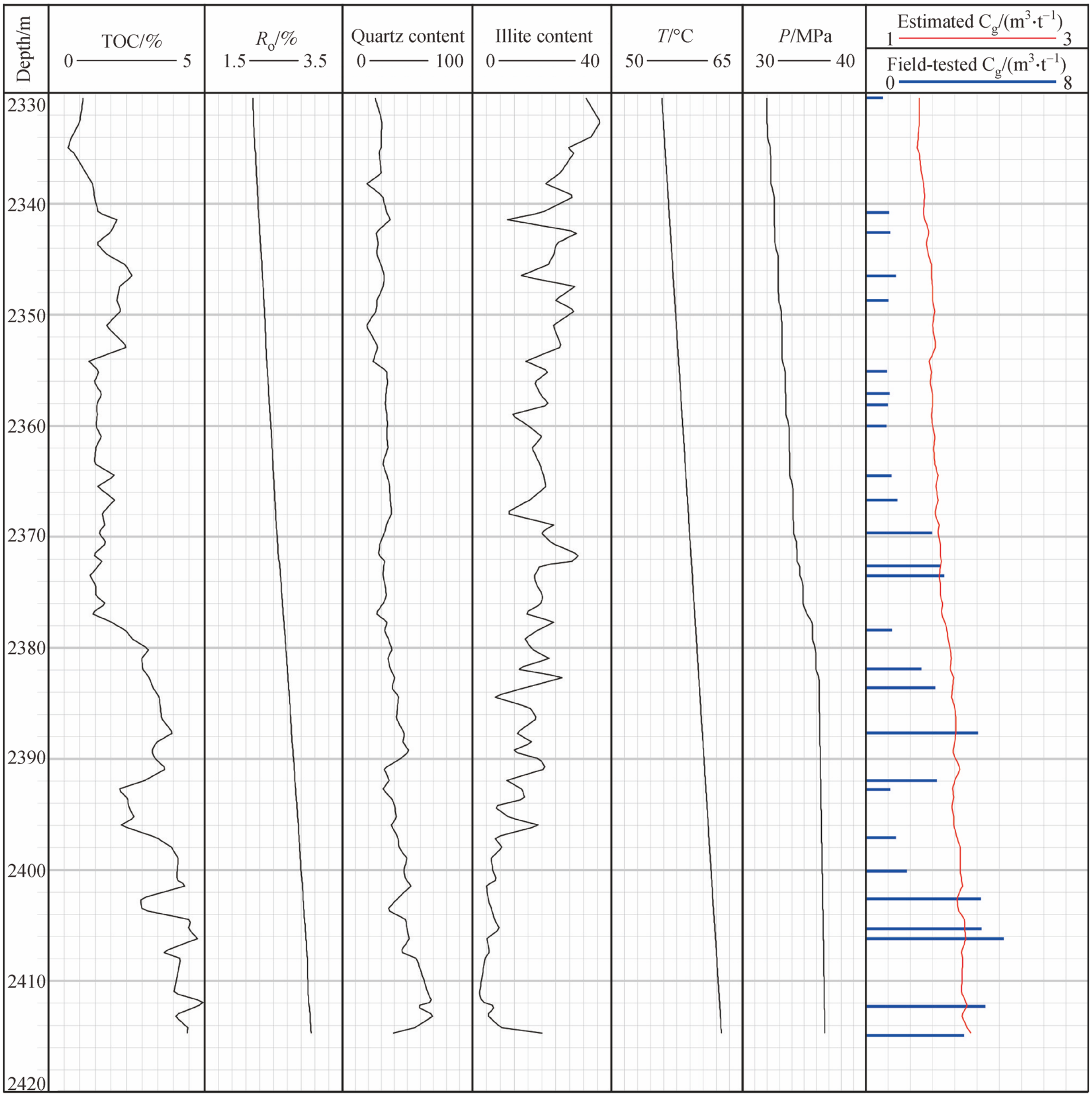

**Fig. 15** Determined methane sorption capacity of the $O_3$w–Lower $S_1$l shale in the JY A well. Formation temperature and pressure are from drilling data. $C_g$ is the gas adsorption capacity.

minerals, is too complicated (Li et al., 2016), which requires more future work to quantitatively establish its impact. Moisture in shale is mainly distributed inside the pores of inorganic minerals such as clay (Chalmers and Bustin, 2010; Li et al., 2016). The correlation between water saturation and TOC and clay minerals of the Wufeng-Longmaxi shale also confirms that the OM and OM pores are oil-wet and pores related to clay minerals are important water storage spaces (Fig. 16). It is reported that when the water saturation of shale is 20%–40%, the methane adsorption capacity drops to about 20% of the dry state (Chalmers and Bustin, 2010). Thus, in this paper, the influence of moisture is reflected in the Eq. (9) and the illite factor is multiplied by 0.2.

The pore structure of shale reservoir also plays an important role in determining methane sorption capacity, since these nano-scale pores have a higher specific surface area, providing more sorption sites (Chalmers and Bustin, 2008; Ross and Bustin, 2009). However, pores in shale reservoirs, e.g., organic pores and matrix pores, are generally governed by TOC, thermal maturity, and minerals. Therefore, we don’t establish a quantitative model to characterize the variation of methane sorption capacity with pore structure.

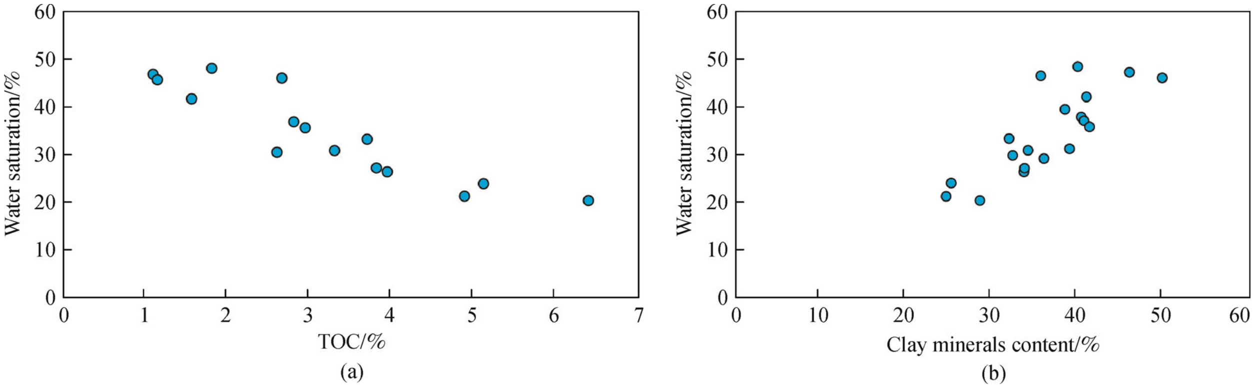

**Fig. 16** The negative correlation between water saturation and TOC (a), and positive correlation between water saturation and clay minerals (b) of the Wufeng-Longmaxi shale.

Individual kerogen types are different in methane sorption capacity, typically increasing in an order: type I < type II < type III kerogen (Zhang et al., 2012). It was attributed to the surface chemistry of different type kerogens, especially aromaticity, e.g., sorption capacity of vitrinite is commonly higher than other maceral types (Zhang et al., 2012). Since evidence from gas carbon isotope and kerogen maceral composition data reveal that $O_3$w–Lower $S_1$l shale is dominated by type I kerogen (Guo et al, 2014), the quantitative expression wasn't established between methane sorption capacity and kerogen type.

## 6 Conclusions

Determination of gas adsorption capacity under geological conditions for organic-rich marine shale is essential in evaluating shale gas resource potential. A quantitative determination of gas adsorption capacity was proposed through 1) investigating controlling geological factors (including both internal ones and external ones) of gas adsorption capacity in organic-rich marine shale with geochemical analysis, XRD diffraction, field-emission scanning electron microscopy, and methane sorption isotherms; 2) defining the relationship between gas adsorption capacity and single controlling factor; 3) establishing a comprehensive determination model with the consideration of all these controlling factors.

The primary controlling factors of the sorption capacity for the studied $O_3$w–Lower $S_1$l shale are TOC, illite and quartz, temperature, pressure. Specifically, TOC, thermal maturity, illite, and pressure are positively correlated with sorption capacity, whereas, quartz and temperature contribute negatively to the sorption capacity.

The application example from the $O_3$w–Lower $S_1$l shale demonstrates that the comprehensive determination model provides a good methane sorption capacity estimation by two criteria, higher correlation coefficients between predicted and measured $C_g$s and biasedness. The correlation coefficient is 0.96, while the residue analysis indicates the model is unbiased statistically.

**Acknowledgements** This study is supported by the National Natural Science Foundation of China (Grant No. 41972160), Open fund of Key Laboratory of oil and gas resources research, Chinese Academy of Sciences (KLOR2018-7). The SINOPEC Exploration Company is thanked for providing data and core samples. The anonymous reviewers are gratefully acknowledged for constructive comments that substantially improved the quality of this manuscript. Also, we appreciate the editor's suggestions to revise this manuscript.

## References

Ambrose R J, Hartman R C, Diaz-Campos M, Akkutlu I Y, Sondergeld C H (2012). Shale gas-in-place calculations, part I: new pore-scale considerations. SPE J, 17(01): 219–229

Chalmers G R L, Bustin R M (2007). The organic matter distribution and methane capacity of the lower cretaceous strata of northeastern British Columbia, Canada. Int J Coal Geol, 70(1–3): 223–239

Chalmers G R L, Bustin R M (2008). Lower cretaceous gas shales in northeastern British Columbia, part I: geological controls on methane sorption capacity. Bull Can Pet Geol, 56(1): 1–21

Chalmers G R L, Bustin R M (2010). The effects and distribution of moisture in gas shale reservoir systems. In: AAPG 2010 Annual Convention and Exhibition, April 11–14

Chen L, Lu Y, Jiang S, Li J, Guo T, Luo C (2015). Heterogeneity of the lower Silurian Longmaxi marine shale in the southeast Sichuan Basin of China. Mar Pet Geol, 65: 232–246

Gasparik M, Bertier P, Gensterblum Y, Ghanizadeh A, Krooss B M, Littke R (2014). Geological controls on the methane storage capacity in organic-rich shales. Int J Coal Geol, 123: 34–51

Gasparik M, Ghanizadeh A, Bertier P, Gensterblum Y, Bouw S, Krooss B M (2012). High-pressure methane sorption isotherms of black shales from the Netherlands. Energy Fuels, 26(8): 4995–5004

Guo X, Li Y, Liu R, Wang Q (2014). Characteristics and controlling factors of micropore structures of the Longmaxi shale in the Jiaoshiba area, Sichuan Basin. Natural Gas Industry B, 1(2): 165–171

Hackley P C, Araujo C V, Borrego A G, Bouzinos A, Cardott B J, Cook

A C, Eble C, Flores D, Gentzis T, Gonçalves P A, Mendonça Filho J G, Hámor-Vidó M, Jelonek I, Kommeren K, Knowles W, Kus J, Mastalerz M, Menezes T R, Newman J, Oikonomopoulos I K, Pawlewicz M, Pickel W, Potter J, Ranasinghe P, Read H, Reyes J, Rosa Rodriguez G D L, Alves Fernandes de Souza I V, Suárez-Ruiz I, Sýkorová I, Valentine B J (2015). Standardization of reflectance measurements in dispersed organic matter: results of an exercise to improve interlaboratory agreement. Mar Pet Geol, 59: 22–34

Hartwig A,Schulz H M (2010). Applying classical shale gas evaluation concepts to Germany—part I: the basin and slope deposits of the Stassfurt Carbonate (Ca2, Zechstein, Upper Permian) in Brandenburg. Geochem, 70(1): 77–91

Hartwig A, Könitzer S, Boucsein B, Horsfield B, Schulz H M (2010). Applying classical shale gas evaluation concepts to Germany—part II: carboniferous in northeast Germany. Geochem, 70(1): 93–106

He C C, He S, Guo X S, Yi J Z, Wei Z H, Shu Z G, Peng N J (2018). Structural differences in organic pores between shales of the Wufeng Formation and of the Longmaxi Formation's first Member, Jiaoshiba Block, Sichuan Basin. Oil & Gas Geol, 39(3): 472–484

Hickey J J, Henk B (2007). Lithofacies summary of the Mississippian Barnett Shale, Mitchell 2 TP Sims well, Wise County, Texas. AAPG Bull, 91(4): 437–443

Hu H, Zhang T, Wiggins-Camacho J D, Ellis G S, Lewan M D, Zhang X (2015). Experimental investigation of changes in methane adsorption of bitumen-free woodford shale with thermal maturation induced by hydrous pyrolysis. Mar Pet Geol, 59: 114–128

Jarvie D M, Hill R J, Ruble T E, Pollastro R M (2007). Unconventional shale-gas systems: the Mississippian Barnett Shale of north-central Texas as one model for thermogenic shale-gas assessment. AAPG Bull, 91(4): 475–499

Ji L, Zhang T, Milliken K L, Qu J, Zhang X (2012). Experimental investigation of main controls to methane adsorption in clay-rich rocks. Appl Geochem, 27(12): 2533–2545

Ji W M, Hao F, Schulz H, Song Y, Tian J (2019). The architecture of organic matter and its pores in highly mature gas shales of the Lower Silurian Longmaxi Formation in the Upper Yangtze Platform, south China. AAPG Bull, 103(12): 2909–2942

Li J, Li X F, Wang X Z, Xin Y N, Han J F, Shi J T, Sun Z, Wang R (2016). Effect of water distribution on methane adsorption capacity in shale clay. Chinese J Theoretic App Mechan, 48(5): 1217–1228 (in Chinese)

Li P, Hao F, Guo X, Zou H, Yu X, Wang G (2015). Processes involved in the origin and accumulation of hydrocarbon gases in the Yuanba gas field, Sichuan Basin, Southwest China. Mar Pet Geol, 59: 150–165

Lu X C, Li F C, Watson A T (1995). Adsorption measurements in Devonian shales. Fuel, 74(4): 599–603

Milliken K L, Rudnicki D, Awwiller D N (2013). Organic matter–hosted pore system, Marcellus formation (Devonian), Pennsylvania. AAPG Bull, 97(2): 177–200

Modica C J, Lapierre S G (2012). Estimation of kerogen porosity in source rocks as a function of thermal transformation: example from the Mowry Shale in the Powder River Basin of Wyoming. AAPG Bull, 96(1): 87–108

Pommer M, Milliken K (2015). Pore types and pore-size distributions across thermal maturity, Eagle Ford Formation, Southern Texas. AAPG Bull, 99(09): 1713–1744

Raut U, Famá M, Teolis B D, Baragiola R A (2007). Characterization of porosity in vapor-deposited amorphous solid water from methane adsorption. J Chem Phys, 127(20): 204713

Ross D J K, Bustin R M (2007). Shale gas potential of the lower Jurassic Gordondale member, northeastern British Columbia, Canada. Bull Can Pet Geol, 55(1): 51–75

Ross D J K, Bustin R M (2008). Characterizing the shale gas resource potential of Devonian–Mississippian strata in the Western Canada sedimentary basin: application of an integrated formation evaluation. AAPG Bull, 92(1): 87–125

Ross D J K, Marc Bustin R (2009). The importance of shale composition and pore structure upon gas storage potential of shale gas reservoirs. Mar Pet Geol, 26(6): 916–927

Schoenherr J, Littke R, Urai J L, Kukla P A, Rawahi Z (2007). Polyphase thermal evolution in the Infra-Cambrian Ara Group (South Oman Salt Basin) as deduced by maturity of solid reservoir bitumen. Org Geochem, 38(8): 1293–1318

Tan J, Horsfield B, Fink R, Krooss B, Schulz H M, Rybacki E, Zhang J, Boreham C J, van Graas G, Tocher B A (2014). Shale gas potential of the major marine shale formations in the upper Yangtze platform, South China, part III: mineralogical, lithofacial, petrophysical, and rock mechanical properties. Energy Fuels, 28(4): 2322–2342

Tian H, Li T, Zhang T, Xiao X (2016). Characterization of methane adsorption on overmature lower Silurian–upper Ordovician shales in Sichuan Basin, southwest China: experimental results and geological implications. Int J Coal Geol, 156: 36–49

Ufer K, Stanjek H, Roth G, Dohrmann R, Kleeberg R, Kaufhold S (2008). Quantitative phase analysis of bentonites by the Rietveld method. Clays Clay Miner, 56(2): 272–282

Wang P, Chen Z, Jin Z, Jiang C, Sun M, Guo Y, Chen X, Jia Z (2018). Shale oil and gas resources in organic pores of the Devonian Duvernay shale, western Canada sedimentary basin based on petroleum system modeling. J Nat Gas Sci Eng, 50: 33–42

Wang P, Chen Z, Pang X, Hu K, Sun M, Chen X (2016). Revised models for determining toc in shale play: example from Devonian Duvernay shale, Western Canada Sedimentary Basin. Mar Pet Geol, 70: 304–319

Wang S, Song Z, Cao T, Song X (2013). The methane sorption capacity of Paleozoic shales from the Sichuan Basin, China. Mar Pet Geol, 44: 112–119

Yang R, He S, Hu Q, Hu D, Zhang S, Yi J (2016b). Pore characterization and methane sorption capacity of over-mature organic-rich Wufeng and Longmaxi shales in the Southeast Sichuan Basin, China. Mar Pet Geol, 77: 247–261

Yang R, He S, Yi J Z, Hu Q H (2016a). Nano-scale pore structure and fractal dimension of organic-rich Wufeng-Longmaxi shale from Jiaoshiba area, Sichuan Basin: investigations using FE-SEM, gas adsorption and helium pycnometry. Mar Pet Geol, 70: 27–45

Zhang T, Ellis G S, Ruppel S C, Milliken K, Yang R (2012). Effect of organic-matter type and thermal maturity on methane adsorption in shale-gas systems. Org Geochem, 47(6): 120–131

Zou C N, Zhai G M, Zhang G Y, Wang H J, Zhang G S, Li J Z, Wang Z M, Wen Z X, Ma F, Liang Y B, Yang Z, Li X, Liang K (2015). Formation, distribution, potential and prediction of global conventional and unconventional hydrocarbon resources. Pet Explor Dev, 42 (1): 14–28